13th International Symposium on Particle Image Velocimetry – ISPIV 2019
Munich, Germany, July 22-24, 2019

Multiscale Proper Orthogonal Decomposition (mPOD) of TR-PIV data: a Case Study on Transient Flows

Miguel A. Mendez[1*], David Hess[2], Bo B. Watz[2], Jean-Marie Buchlin[1]

[1] von Karman Institute for Fluid Dynamics, Sint-Genesius-Rode, Belgium

[2] Dantec Dynamics AS, Denmark

[*] mendez@vki.ac.be

Abstract

Data-driven decompositions of Particle Image Velocimetry (PIV) measurements are widely used for a variety of purposes, including the detection of coherent features (e.g., vortical structures), filtering operations (e.g., outlier removal or random noise mitigation), data reduction and compression. This work presents the application of a novel decomposition method, referred to as Multiscale Proper Orthogonal Decomposition (mPOD, Mendez et al 2019) to Time-Resolved PIV (TR-PIV) measurement. This method combines Multiresolution Analysis (MRA) and standard Proper Orthogonal Decomposition (POD) to achieve a compromise between decomposition convergence and spectral purity of the resulting modes. The selected test case is the flow past a cylinder in unsteady conditions, featuring a frequency-varying Karman vortex street. The results are compared to those obtained via classical POD in terms of decomposition convergence as well as spatial and time-frequency localization.

1 Introduction and Motivation

Data-driven decompositions of PIV measurements are nowadays part of the standard toolbox for post-processing techniques used to extract knowledge from experimental data. Originally developed for identifying coherent structures in turbulent flows (Sirovich, 1987, 1989; Holmes et al., 1997) these decompositions have found applications also as random noise removal (Raiola et al., 2015), image pre-processing tools (Mendez et al., 2017), model order reduction for advanced active flow control (Berger et al., 2014; Brunton and Noack, 2015) and for validation of numerical simulations (Erik et al., 2007).

Although several variants exist (see Taira et al. 2017; Rowley and Dawson 2017; Amor et al. 2019 for a review), the two fundamental decompositions are the Proper Orthogonal Decomposition (POD, Sirovich (1987); Lumley (1970)) and the Dynamic Mode Decomposition (DMD, Schmid (2010); Rowley et al. (2009)). The first is based on the energy optimality formulation, so that the POD provides the most energetic modes with no constraints on their frequency content; the second is based on the spectral purity formulation, so that the DMD provides the best harmonic modes describing the data.

Both the constraints of energy optimality and spectral purity are often unnecessary, as discussed by Mendez et al. (2019), and research on data-driven decompositions is currently focused on the development of hybrid methods (see Noack 2016). Spectral Proper Orthogonal Decomposition (Sieber et al., 2016), Multiresolution Dynamic Mode Decomposition (Kutz et al., 2016b), Recursive Dynamic Mode Decomposition (Noack et al., 2016) or Cronos-Koopman analysis (Cammilleri et al., 2013) are some successful examples of decompositions aiming at bridging spectral purity and energy optimality. These methods propose ingenious combinations of POD and DMD of various degrees of complexity and are designed for data sets that are statistically stationary (hinging on the time-frequency duality of the POD) or have short-duration departures from fixed points (hinging on the linearization of the dynamics in the DMD). For datasets featuring more complex transitory, e.g. having one or more growth/decay saturation, impulsive events (that are not easily represented by harmonic decompositions nor linear dynamical systems) or phenomena having similar energy content (that leads to non-unique POD), these methods lose their theoretical fundamentals and yields poor feature detection capabilities.

A flexible and robust approach to study such kind of datasets is the Multiscale Proper Orthogonal Decomposition (mPOD) proposed by Mendez et al. (2018b, 2019). The mPOD combines Multi-resolution Analysis (MRA) via filter banks and POD. The MRA is used to decompose the correlation matrix of the

data into the contribution of different scales, each retaining non-overlapping portions of the frequency spectra and leading to a POD constrained within the corresponding frequency bandwidth. The set of POD of each scale is then used to assemble the mPOD basis, which is kept orthogonal by construction.

After a brief review of the mPOD algorithm in Sec.2, this work presents the mPOD analysis of an exemplary TR-PIV test case and a comparison of its performances with those of classical POD in terms of feature detection and time-frequency localization capabilities while the decomposition convergence is compared also to classical Discrete Fourier Transform (DFT). Sec.3 presents the experimental setup and selected test case: the flow past a cylinder in accelerating conditions, producing a vortex shedding with varying frequency. The results are discussed in Sec.4, while conclusions and perspectives are reported in Sec.5.

2 The Multiscale Proper Orthogonal Decomposition

All the data-driven decompositions discussed in this work break a discrete dataset, here the velocity field $\vec{u}(\mathbf{x},t)$ produced by TR-PIV measurements, into the sum of $n_t < n_s$ modes, with n_s the number of spatial points in and n_t the number of time steps (measurements). These modes have spatial structures $\vec{\phi}_k$, which can be seen as dominant spatial patterns in the flow, temporal structure ψ_k, that controls their evolution, and an energy contribution σ_r, that weights their importance. The mPOD, POD and DMD/DFT modes are distinguished using the subscripts $\mathcal{M}$, $\mathcal{P}$ and $\mathcal{D}$ respectively. No subscripts are used in equations that hold for all the decompositions.

It is important to highlight that it is not possible to define spatial and temporal structures independently since one univocally identifies the other. Focusing on the identification of the temporal structures as bases for the temporal evolution of the data, and assuming that these are orthogonal (uncorrelated), any decomposition can be written in two equivalent forms:

$$\vec{u}(\mathbf{x},t) = \sum_{r=1}^{n_t} \sigma_r \vec{\phi}_r(\mathbf{x})\,\psi_r(t) = \sum_{r=1}^{n_t} \left\langle \vec{u}(\mathbf{x},t)\,,\psi_r(t) \right\rangle_T \psi_r(t) \tag{1}$$

where $\langle , \rangle_T$ denotes the chosen inner product (typically a standard L^2). The second form on the right-hand side replaces the spatial structure by their definition, that is a set of n_s projections of the dataset evolution in each spatial point $\mathbf{x}$ onto the corresponding temporal structure.

A third representation consists in keeping the spatial structures in the summation and replacing the temporal ones with their definition as a projection of the datasets onto the spatial basis. This, however, requires that the spatial structures are orthogonal. In the case of the POD, for which this is the case, these two forms are equivalent (see Aubry (1991)) and preferring the first over the second is only a matter of memory saving. In the case of DMD or mPOD, this is symmetry does not hold: these decompositions identify coherent patterns from their temporal evolution and only in a second step, via time projection, in the spatial domain.

The temporal structures of the POD modes $\psi_{\mathcal{P}k}$ are eigenvectors of the temporal correlation matrix $K_{i,j} = \langle \vec{u}(\mathbf{x},t_i), \vec{u}(\mathbf{x},t_j) \rangle_T$ (Sirovich, 1987). Arranging eq.(1) as a matrix decomposition, it is easy to see that the POD of a dataset with a uniform spatial and temporal grid (as in classical TR-PIV data) is equivalent to the Singular Value Decomposition (SVD) of the data rearranged as a single matrix. By definition, the POD yields the optimal basis, in the sense that the error produced by cutting the summation in eq.(1) to $r_c < n_t$ modes is the minimum possible:

$$\mathcal{E}(r_c) = \frac{||\vec{u}(\mathbf{x},t) - \sum_{r=1}^{r_c} \left\langle \vec{u}(\mathbf{x},t)\,,\psi_r(t) \right\rangle_T \psi_r(t)||_2}{||\vec{u}(\mathbf{x},t)||_2} \tag{2}$$

where $||\bullet||_2$ denotes the L_2 norm. It is moreover possible to show that $\mathcal{E}(r_c) = \sigma_{\mathcal{P}r_c+1}$, $||\vec{u}(\mathbf{x},t)||_2 = \sigma_{\mathcal{P}1}$ and $\sigma_{\mathcal{P}_k} = \sqrt{\lambda_k}$, with λ_k the eigenvalues of the correlation matrix K. By construction, the POD yields optimal convergence, fast evaluation of the decomposition error and perfect symmetry between temporal and spatial structures, which allows for fast algorithms for its computation (see Sirovich (1987)). However, as discussed in previous contributions (Mendez et al., 2019, 2018b), major problems occur when different phenomena have similar energy content, resulting in nearly repeated eigenvalues λ_r and thus a non-unique decomposition. The lack of any constraint on the frequency content of its modes, combined with the requirement for energy optimality and non-uniqueness problems, these circumstances leads to spectral mixing between the modes as illustrated also in the test case presented in Sec.4.

The temporal structures of the DMD modes $\psi_{\mathcal{D}k}$ are complex exponentials with (complex) frequency obtained from the eigenvalues of the linear dynamical systems which better approximates the datasets (Budišić et al., 2012; Chen et al., 2012). This dynamical system is identified by a propagator matrix $\mathcal{P}$, which can be computed from the dataset using classical inverse methods. Since such propagator is usually of prohibitively large dimensions, standard DMD algorithms rely on a low order approximation of it (Schmid, 2010) or adaptations of the well known Arnoldi algorithm (Rowley et al., 2009) for the numerical calculation of its eigenvalues. A detailed overview of the variants of DMD algorithms and their application is provided by Kutz et al. (2016a). The major advantage of the DMD is to provide modes that are harmonic but do not suffer from the limitations of the classical Fourier Modes: the frequencies in the DMD are inferred from the data and not defined a priori as integer multiples of a fundamental tone. Therefore, the DMD does assume that the data-set is periodic and hence does not suffer from frequency leaking problems (Harris, 1978). Moreover, frequencies are allowed to be complex (as in the Z-transform), making DMD modes well suited for describing exponentially decaying or growing phenomena. Because of the underlying assumption of linear dynamics, however, the DMD is incapable of describing nonlinear dynamics such as growth/decay saturation, and, because of the constraints of harmonic modes, it is equally incapable of providing time localization. In the test case investigated in this work, neither the classical Companion based nor the SVD based algorithm proved successful in decomposing the data. In particular, both formulations yields strongly decaying exponential modes which in this case yields non-invertible temporal structure matrix $\Psi_{\mathcal{D}}$. To evaluate the convergence of a harmonic decomposition, the DMD is performed after subtracting the temporal average, thus reducing the decomposition to the classical DFT Chen et al. (2012).

The Multiscale Proper Orthogonal Decomposition (mPOD) proposed in Mendez et al. (2018b, 2019) presents a compromise between the POD and the DMD by adding spectral constraints to the energy optimality of the POD. Following the classical Multi-Resolution Analysis (MRA) formulation common in Wavelet theory (Mallat, 2009), the mPOD starts by breaking the temporal correlation matrix K into the contribution of M scales. These scales are obtained by a bank of 2D filters, with transfer function $\mathcal{H}_m$, which isolate the spectral content of the correlation matrix into non-overlapping portions, and such that the full energy content is preserved. This is obtained by constructing the transfer functions such that $\sum_m^M \mathcal{H}_m = \underline{1}$, and $\mathcal{H}_i \odot \mathcal{H}_j = 0 \forall i \neq j$, where $\underline{1} \in \mathbb{R}^{n_t \times n_t}$ is the unitary matrix and $\odot$ is the Shur (entry by entry) product.

For symmetric filters, these contribution preserves the symmetry of the full correlation matrix and are therefore equipped with n_m orthogonal eigenvectors:

$$K = \sum_{m=1}^{M} K_m = \sum_{m=1}^{M} \Psi_{\mathcal{F}} \left[\widehat{K} \odot \mathcal{H}_m \right] \Psi_{\mathcal{F}} = \sum_{m=1}^{M} \left(\sum_{r=1}^{n_m} \lambda_r^{(m)} \psi_{\mathcal{M}r} \psi_{\mathcal{M}}^{(m)^T} \right) \tag{3}$$

where $\Psi_{\mathcal{F}} \in \mathbb{C}^{n_t \times n_t}$ is the Fourier matrix $\Psi_{\mathcal{F}}[i,j] = exp(2\pi \mathrm{j}/n_t)^{(i-1)\times(j-1)}$, with $i,j = [1,n_t]$, and $\widehat{K} = \overline{\Psi}_{\mathcal{F}} K \overline{\Psi}_{\mathcal{F}}$ is the 2D Fourier transform of the correlation matrix, with over-line denoting complex conjugation. If no frequency overlapping occurs, it is possible to show (see Mendez et al. (2019)) that the eigenvectors in each of the m scales are mutually orthogonal and therefore are orthogonal complements spanning the entire $\mathbb{R}^{n_t}$ space (that is $\sum_{m=1}^{M} n_m \approx n_t$). Therefore, the mPOD algorithm constructs the temporal basis by sorting the structures in each scale in order of energy contribution, defined by the corresponding eigenvalues $\lambda_r^{(m)}$ regardless of their scale of origin.

The filter bank can be constructed using Dyadic Wavelet decomposition (as in Mendez et al. (2018a,b)) or more generally using a set of filters with user-defined band-pass widths (as in Mendez et al. (2019)). In this work, these are constructed as standard FIR filters, designed via windowing method (Oppenheim and Schafer, 2009). The resulting decomposition has convergence that is comparable to the POD while maintaining the frequency spectra of all its modes reasonably band-limited. Moreover, the MRA architecture lets the mPOD recover the energy optimality of the POD at the limit of a single scale (spanning the entire frequency range), and the spectral purity of the DMD at the limit of n_t scales (each taking one frequency bin).

3 Experimental Set Up and Selected Test Case

The selected test case is the flow past a cylinder of 5 mm diameter in transient conditions, with varying free stream velocity. The experiments were carried out in the L10 low-speed wind tunnel of the von Karman Institute, instrumented with a TR-PIV system from Dantec Dynamics. The tunnel has a cross section of 20cm×20cm and is equipped with a piezo resistive pressure transducer AMS5812 to monitor the pressure in the honeycomb chamber. A Laskin Nozzle PIVTEC45-M, operating with the mineral oil Ondina Shell

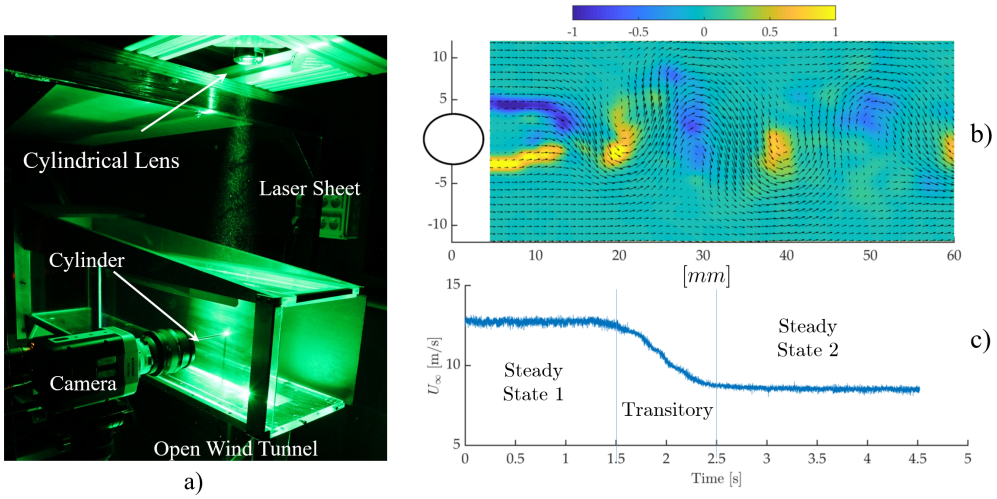

Figure 1: Fig a) Picture of the experimental set up during an TR-PIV measurement. Fig b) Instantaneous velocity field and normalized vorticity (that is scaled between $[-1,1]$). Fig c) time evolution of the free stream velocity U_∞, taken from a point far from the cylinder surface.

91, is used to produce seeding particles of about $1.5\mu m$ in diameter, injected in the intake manifold of the wind tunnel fan.

The flow is studied with a time-resolved PIV system from Dantec Dynamics. The particles are illuminated with a Physics Instruments Nd:YLF laser offering 20 mJ/pulse at 1 kHz. The exposed scene of about 70×26 mm is recorded by a SpeedSense 9090 camera offering 7500 fps at a resolution of 1280×800 px. To extend the measurement duration, the sensor is cropped to 1280×720 px resulting in about $n_t = 13500$ double frames, thus, covering a sequence of about 4.5 seconds. A picture of the experimental set-up is shown in Figure 1a).

For acquisition and analysis, DynamicStudio is used. For the initial data processing, standard adaptive PIV (see Theunissen (2010)) is used with an initial interrogation area of 96 x 96 px and final size of 24 x 24 px, the vectors are calculated every 12 px resulting in an overlap of 50%. Before the mPOD analysis, the only filter applied is universal outlier detection with a filter kernel of $3x3$ vectors, as suggested by Westerweel and Scarano (2005). An example of instantaneous velocity is shown in Figure 1b, together with the normalized vorticity field. In the investigated test case, the velocity of the free stream U_∞ evolves through two steady state conditions, namely from $U_\infty \approx 14$ to $U_\infty \approx 8$ m/s, as shown in Figure 1c). The transition between these is a smooth step of approximately $1s$. The Reynolds number varies from $Re = 4980$ to $Re = 3070$ and the frequency of the vortex shedding varies from $459Hz$ to $303Hz$, corresponding to a Strouhal number of about $St = f\,d/U_\infty = 0.16$ in both stationary regimes.

4 Results

The convergence error in eq.(2) is shown in Figure 2 for the POD, the mPOD and the DFT. The DFT is computed taking the columns of the Fourier matrix $\Psi_\mathcal{F}$ as temporal structures in eq.(1), and is equivalent to performing the DMD on the mean-shifted dataset.

The convergence of the DFT is much weaker than the optimal POD, because of the spectral leakage due to the non-periodic extension of the data. The mPOD performs considerably better than the DFT, reaching negligible convergence errors for $r_c > 6$. This is close to the optimal limit, defined by the POD, which yields almost no reconstruction error for $r_c > 3$. It is worth noticing that the mPOD convergence becomes particularly poor for $r_c > 6$ because a broad range of frequencies ($f > 500Hz$) is removed from the data.

To study the main differences between the POD and the mPOD, it is worth exploring the frequency spectra of the temporal correlation matrix and how the mPOD partitions its content among the various modes. Fig.3 a) shows the contour of the magnitude of the Fourier transformed correlation matrix $\widehat{K}$. The dominant frequencies at $\approx 303Hz$ and $\approx 459Hz$, corresponding to the vortex shedding in the two steady states, are evident along the diagonal of this matrix. Because of the finite frequency resolution, the correlation between these two phenomena, occurring at different frequencies, extends to the off-diagonal regions and creates

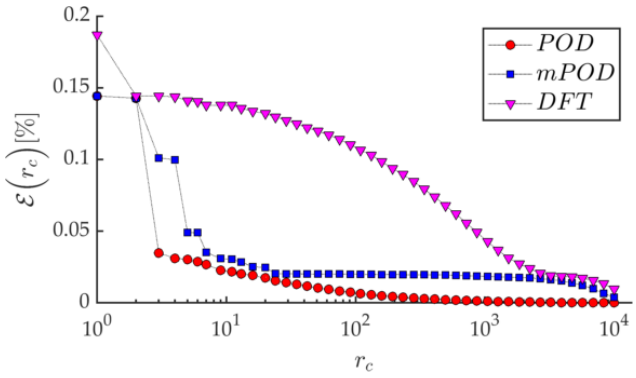

Figure 2: Convergence error from eq.(2) for the POD, mPOD and the DFT.

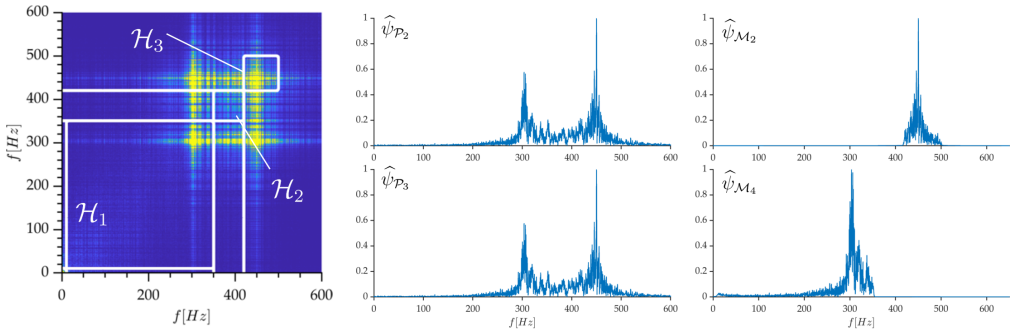

a) b) c)

Figure 3: Left: contour map of the magnitude of the Fourier transformed correlation matrix $\widehat{K}$, showing two dominant peaks at $\approx 303Hz$ and $\approx 459Hz$ and the boundaries of the identifies mPOD scales (white lines). The first two POD modes capture both frequencies in the same modes (the second and the third), while the mPOD assigns different modes to these two dominant harmonics.

secondary peaks linked to their reciprocal correlation.

Following the constraint of energy optimality, the POD assigns both frequencies to the same modes: the second and the third. The frequency spectra of the temporal structure of these modes are shown in Fig.3 b). These modes have identical spatial and temporal structures, phase shifted in time and space, to describe the traveling wave nature of the vortex shedding.

The mPOD used in this work is composed of four scales, defined to separate, respectively, (1) the large scale evolution of the free stream velocity, the vortex shedding at the high (2) and the low (3) free stream velocity and (4) the transition between these two. The frequency interval assigned to these four scales are (1) $[0-10]Hz$, (2) $[10-350]Hz$, (3) $[350-420]Hz$ and (4) $[420-500]Hz$. Frequencies higher than $500Hz$ are filtered out from the decomposition.

As described in Mendez et al. (2019), the transfer functions isolating these contributions are centered along the diagonal of $\widehat{K}$ and defines square regions. The boundaries of these regions are shown in Fig.3a): the largest scale $\mathcal{H}_L$ captures the lowest range ($f < 10Hz$), the first intermediate scale $\mathcal{H}_1$, taking the second range, includes the harmonic contribution of the vortex shedding at the lowest frequency. The highest scale $\mathcal{H}_3$ is focused on the frequency of the vortex shedding at the highest velocity, while the intermediate range, corresponding to the transitory between these two, is taken by $\mathcal{H}_2$.

It is essential to observe that these spectral constraints only impose that a mode having frequency content in one scale does not have frequency content in others. Each scale is equipped with its POD, and the final mPOD basis is constructed by sorting these POD from various scales by energy contribution (associated eigenvalue). The spectra of two representative mPOD modes, namely the second and the fourth, are shown in Fig.3(c). Being mPOD modes real and associated with traveling structures, both of these modes have their phase-shifted counterpart (the third and the fifth mode respectively) with equal frequency.

Figure 4 shows the spatial and the temporal structures of the first mode for the POD (left) and the mPOD

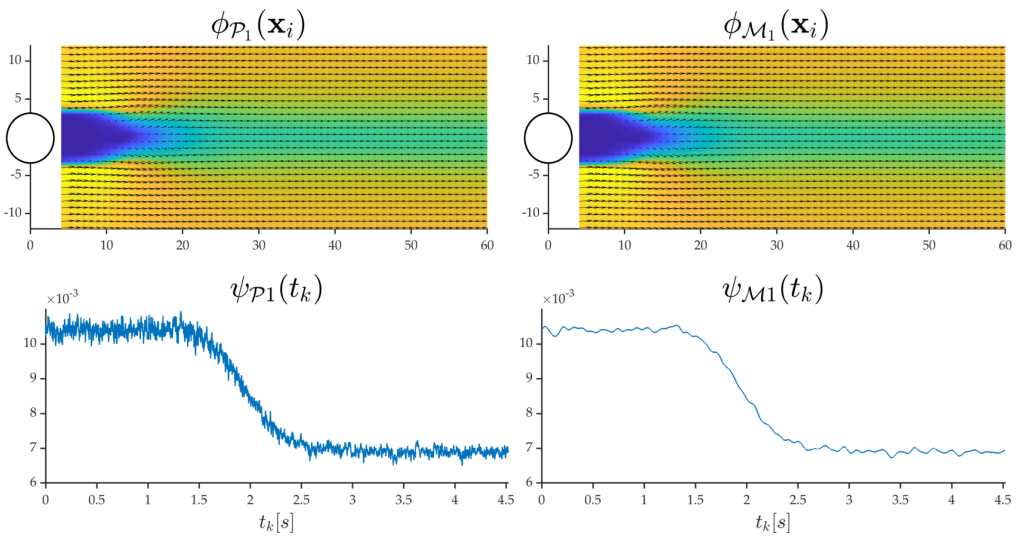

Figure 4: Spatial and temporal structures of the dominant POD (left) and mPOD (right) modes. Both modes capture the large scale evolution of the free stream flow. However, while the POD mode is influenced by noise and higher frequency contribution, the mPOD mode is more focused on the large scale variations in the flow.

(right). Both decompositions identify as dominant mode the large scale variations of the velocity field, with temporal structure essentially reproducing the velocity in the far field conditions as shown in Fig.1c). In the case of the POD, however, random and higher frequency contributions are also captured by this mode: as extensively described in Mendez et al. (2017), random noise is equally distributed among all the POD modes. The frequency constrained mPOD mode is, on the other hand, more focused on the large scale variations and almost entirely free of random noise.

Figure 5 shows the spatial structure of three representative modes, together with the Continuous Wavelet Transform (CWT) of their corresponding temporal structure. The second POD mode, along with its phase-shifted counterpart (third mode) and the first mode, describes the entire dataset with negligible error (see also Fig.2). Therefore, this mode captures the whole evolution of the vortex shedding, and the CWT of its temporal structure display the footprint of the evolution of the free stream velocity (see also Fig.1c).

It is therefore not possible to understand how much the spatial structure of this mode is linked to the vortex shedding at the highest or the lowest frequency, or to the transitory between the two: to capture as much energy as possible with the minimum number of modes, the POD describe *all* these features with only two phase-shifted modes. The spatial structure is, therefore, a linear combination of the spatial structures that one could associate to each of these independently. The fourth and the fifth modes, having negligible energy contribution (see Fig.2), have a temporal structure with a broad range of frequencies, spread over the entire duration of the experiment.

On the contrary, the mPOD modes have a precise localization in the frequency and in the time domain. In particular, the second/third modes are linked to the vortex shedding in the first $1.5s$ of the experiment, namely at the highest velocity (see Fig.1c), while the fourth/fifth modes are related to the vortex shedding at $t > 2s$, namely at the lowest frequency. These mPOD modes are POD modes of the scales isolated by $\mathcal{H}_3$ and $\mathcal{H}_1$ respectively. The sixth mode is linked to the transitory between the two and originates from the scale isolated by $\mathcal{H}_2$.

To analyze how well these modes describe the vortex shedding occurring in the initial and the final part of the experiment, Figure 6 compares the error produced by low-rank approximations using only mPOD modes with the error produced by low-rank approximation using POD modes. In particular, $E_{2,3}$ refers to the normalized L_2 error that the mPOD modes 2 and 3 produce with respect to the POD modes 2 and 3. It is clear that these two mPOD modes are aligned to the POD only in the first part of the dataset, in which the high-frequency shedding is produced. Similarly, $E_{4,5}$ refers to the normalized L_2 error that the mPOD modes 4 and 5 produce with respect to the POD modes 2 and 3, and show that these are well aligned with the POD modes in the second part of the dataset, in which the low frequency is produced. To conclude, the POD modes capture multiple features, and it is not possible to distinguish how its spatial structures are linked to one or the other. The mPOD separates the various mechanisms and assigns a different mode to

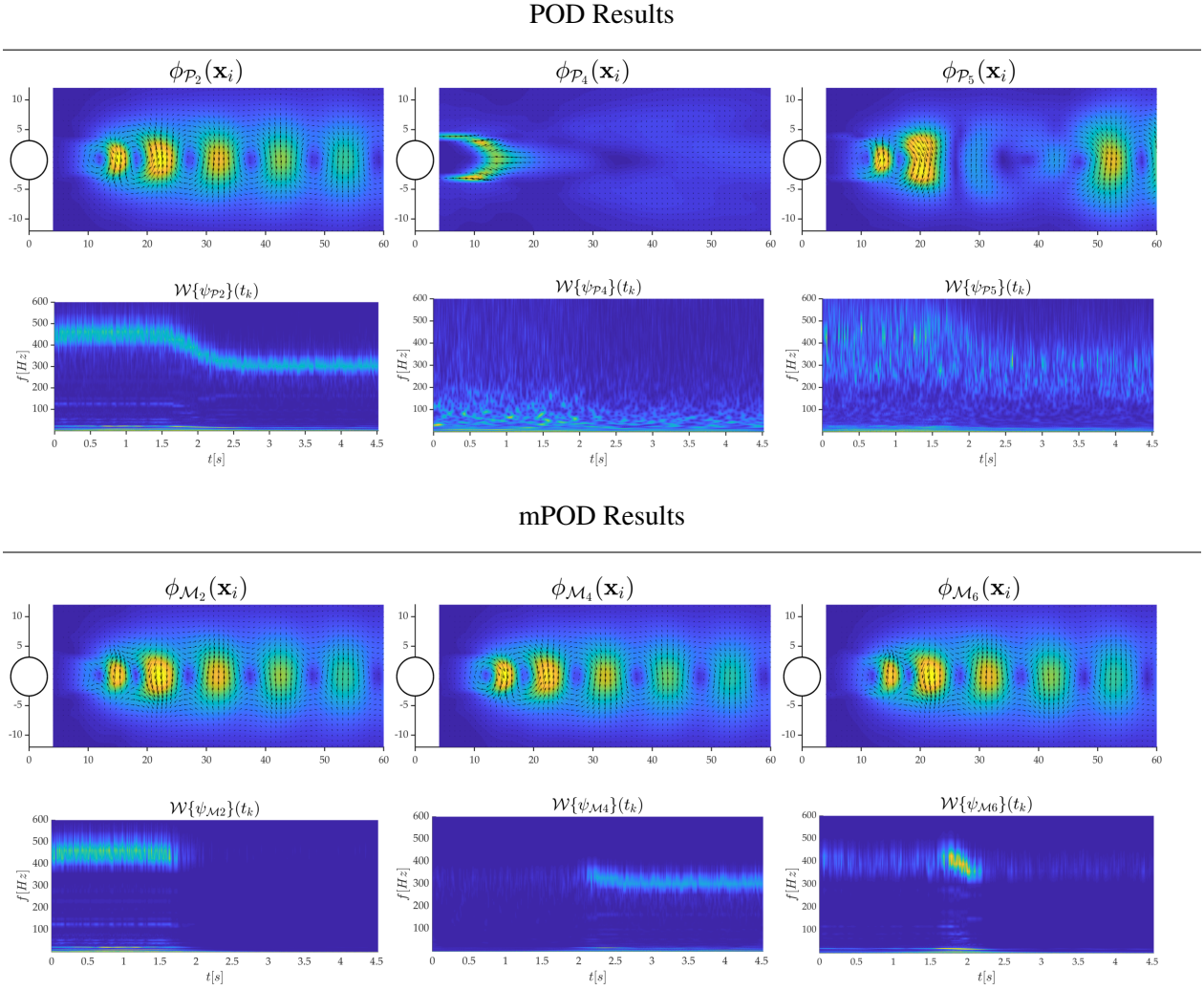

Figure 5: Decomposition of the TR-PIV acquisition of the accelerating flow past a cylinder: spatial (ϕ) and temporal (ψ) structures of the three dominant POD (top) and mPOD modes (bottom). For the first mode, the temporal structures are shown in the time domain; for the others, these are shown in the time-frequency domain using a CWT.

each of them, without significantly losing in decomposition convergence as it occurs to the harmonic DFT or, worse, to the DMD.

5 Conclusions

The Multiscale Proper Orthogonal Decomposition (mPOD) has been tested on the Time-Resolved PIV measurements of a canonical flow past a cylinder in transitory conditions. This transitory is obtained by decreasing the velocity profile of the free stream and thus varying the frequency of the vortex shedding between two well-defined values.

The performances of the mPOD are compared to those of a Proper Orthogonal Decomposition (POD) and the Discrete Fourier Transform (DFT), while two classical algorithms for the Dynamic Mode Decomposition (DMD), namely the Companion based and the SVD based formulations proved unsuccessful. Specifically, due to the nonlinear nature of the test case, all the complex exponential vanishes within a few time steps and leads to a severely ill-conditioned projection problem. The standard DFT, which can be seen as a DMD on mean-substracted data, yields poor decomposition because of the non-harmonic extension of the data.

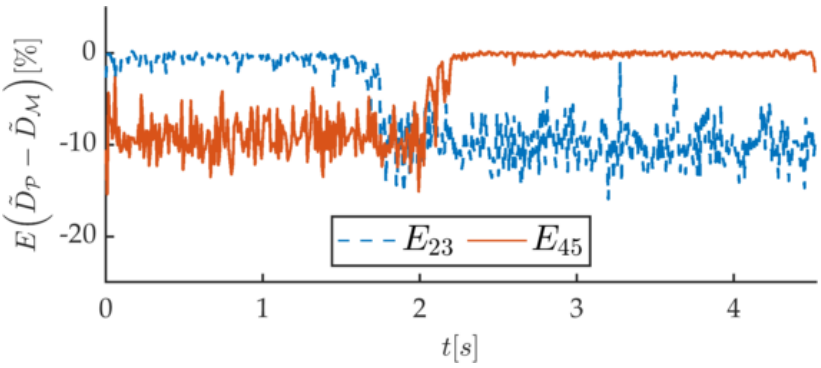

Figure 6: Difference in the reconstruction error produced by the mPOD modes 2 and 3 ($E_{2,3}$) and the mPOD modes 4 and 5 ($E_{4,5}$), with respect to the POD modes 2 and 3. Clearly, the first mPOD modes are aligned to the POD ($E_{2,3} \approx 0$) in the first 1.6s while the reverse is true afterwards.

The optimal convergence of the POD results in the opposite problem, with only three modes describing the entire dataset. This is achieved at the cost of assigning to a single mode (and its phase-shifted counterpart) the whole evolution of the vortex shedding. The corresponding spatial structures are consequently a mix of features from these different phases of the flow evolution, which becomes therefore indistinguishable.

The spectral constraints of the mPOD allow for distinguishing the various steps in the evolution of the dataset both in the time and the frequency domains, assigning different modes accordingly. Thanks to the MRA architecture, this is achieved with a minor loss in the decomposition convergence with respect to the optimal POD.

References

Amor C, Pérez JM, Schlatter P, Vinuesa R, and Clainche SL (2019) Soft computing techniques to analyze the turbulent wake of a wall-mounted square cylinder. in *Advances in Intelligent Systems and Computing*. pages 577–586. Springer International Publishing

Aubry N (1991) On the hidden beauty of the proper orthogonal decomposition. *Theor Comput Fluid Dyn* 2:339–352

Berger ZP, Shea PR, Berry MG, Noack BR, Gogineni S, and Glauser MN (2014) Active flow control for high speed jets with large window PIV. *Flow, Turbulence and Combustion* 94:97–123

Brunton SL and Noack BR (2015) Closed-loop turbulence control: Progress and challenges. *Applied Mechanics Reviews* 67:050801

Budišić M, Mohr R, and Mezić I (2012) Applied koopmanism. *Chaos: An Interdisciplinary Journal of Nonlinear Science* 22:047510

Cammilleri A, Gueniat F, Carlier J, Pastur L, Memin E, Lusseyran F, and Artana G (2013) POD-spectral decomposition for fluid flow analysis and model reduction. *Theor Comput Fluid Dyn* 27:787–815

Chen KK, Tu JH, and Rowley CW (2012) Variants of dynamic mode decomposition: Boundary condition, koopman, and fourier analyses. *Journal of Nonlinear Science* 22:887–915

Erik MK, Dalibor C, and M PJ (2007) Pod as tool for comparison of piv and les data. in *7th International Symposium on Particle Image Velocimetry*. Rome, Italy

Harris F (1978) On the use of windows for harmonic analysis with the discrete fourier transform. *Proc IEEE* 66:51–83

Holmes PJ, Lumley JL, Berkooz G, Mattingly JC, and Wittenberg RW (1997) Low-dimensional models of coherent structures in turbulence. *Phys Rep* 287:337–384

Kutz JN, Brunton SL, Brunton BW, and Proctor JL (2016a) *Dynamic Mode Decomposition: Data-Driven Modeling of Complex Systems*. SIAM-Society for Industrial and Applied Mathematics

Kutz JN, Fu X, and Brunton SL (2016b) Multiresolution dynamic mode decomposition. *SIAM J Appl Dyn Syst* 15:713–735

Lumley JL (1970) *Stochastic Tools in Turbulence*. DOVER PUBN INC

Mallat S (2009) *A Wavelet Tour of Signal Processing*. Elsevier LTD, Oxford

Mendez M, Raiola M, Masullo A, Discetti S, Ianiro A, Theunissen R, and Buchlin JM (2017) POD-based background removal for particle image velocimetry. *Experimental Thermal and Fluid Science* 80:181–192

Mendez MA, Balabane M, and Buchlin JM (2018a) Multi-scale proper orthogonal decomposition (mPOD). in *AIP Conference Proceedings*

Mendez MA, Balabane M, and Buchlin JM (2019) Multi-scale proper orthogonal decomposition of complex fluid flows. *Journal of Fluid Mechanics* 870:988–1036. Preprint available at `https://arxiv.org/abs/1804.09646`.

Mendez MA, Scelzo M, and Buchlin JM (2018b) Multiscale modal analysis of an oscillating impinging gas jet. *Experimental Thermal and Fluid Science* 91:256–276

Noack BR (2016) From snapshots to modal expansions – bridging low residuals and pure frequencies. *J Fluid Mech* 802:1–4

Noack BR, Stankiewicz W, Morzyński M, and Schmid PJ (2016) Recursive dynamic mode decomposition of transient and post-transient wake flows. *J Fluid Mech* 809:843–872

Oppenheim A and Schafer RW (2009) *Discrete-Time Signal Processing [With Access Code]*. ADDISON WESLEY PUB CO INC

Raiola M, Discetti S, and Ianiro A (2015) On PIV random error minimization with optimal POD-based low-order reconstruction. *Experiments in Fluids* 56

Rowley C, Mezić I, Bagheri S, Schlatter P, and Henningson D (2009) Spectral analysis of nonlinear flows. *J Fluid Mech* 641:115

Rowley CW and Dawson ST (2017) Model reduction for flow analysis and control. *Annu Rev Fluid Mech* 49:387–417

Schmid P (2010) Dynamic mode decomposition of numerical and experimental data. *J Fluid Mech* 656:5–28

Sieber M, Paschereit CO, and Oberleithner K (2016) Spectral proper orthogonal decomposition. *J Fluid Mech* 792:798–828

Sirovich L (1987) Turbulence and the dynamics of coherent structures: Part i. coherent structures. *Quart Appl Math* 45:561–571

Sirovich L (1989) Chaotic dynamics of coherent structures. *Physica D* 37:126–145

Taira K, Brunton SL, Dawson STM, Rowley CW, Colonius T, McKeon BJ, Schmidt OT, Gordeyev S, Theofilis V, and Ukeiley LS (2017) Modal analysis of fluid flows: An overview. *AIAA J* 55:4013–4041

Theunissen R (2010) *Adaptive resolution in PIV image analysis - Application to complex flows and interfaces*. Ph.D. thesis. von Karman Institute for Fluid Dynamics & Technische Universiteit Delft, The Netherlands & Vrije Universiteit Brussel, Belgium,

Westerweel J and Scarano F (2005) Universal outlier detection for PIV data. *Experiments in Fluids* 39:1096–1100